A Multiple-Grid Scheme for Solving the Euler Equations

Ron-Ho Ni*

Pratt & Whitney Aircraft Group, East Hartford, Connecticut

A fast, explicit numerical scheme for solving the unsteady Euler flow equations to obtain steady solutions is presented. The scheme is constructed by combining the multiple-grid technique with a new second-order accurate finite volume integration method. Special formulas, consistent with local wave propagations, are utilized to determine corrections of flow properties at each grid point. These formulas are found to provide useful insights into the solution procedure. Calculated results for both internal and external flow problems are given to demonstrate the accuracy and computational efficiency of this scheme.

Introduction

A EULER flow solver is needed for a variety of reasons, such as for the case of providing a unique shock solution for flow in converging-diverging passages formed by turbomachinery blades, the case of determining the rotational flowfield behind a strong shock standing on a wing or nacelle operated at off-design condition, etc. Due to the simplicity both in physical interpretation and numerical implementation, explicit time marching procedures[1-3] are generally used to solve the Euler equations. However, the computational time required by those procedures to arrive at an accurate solution is often prohibitive. There are methods for speeding up the computation. Higher order approximation[4] and multiple-grid technique[5] are among them. In this study, the multiple-grid concept is utilized and combined with a newly developed second-order integration method to form a fast and accurate explicit Euler solver.

To model the law of conservation, the new integration method utilizes non-overlapping control volumes for the spatial approximation to the governing equations. To provide the proper domain of dependence, special formulas called "distribution" formulas are used for determining the corrections ($\delta U = U^{n+1} - U^n$) to the grid points. These formulas are derived from a one-step second-order explicit procedure for solving hyperbolic equations and have been found to be consistent with local wave characteristics. The new method is second-order accurate in time.

In the multiple-grid application, the corrections to the fine grid points are transferred to coarser grids to maintain the low truncation errors associated with fine level of discretizations. The distribution formulas are used to propagate the changes onto the coarser grid points. After applying interpolation to the coarse grid corrections, the flow properties at every point of the finest mesh are updated. It requires less numerical work for propagating the waves on the coarser grids, so the use of the multiple-grid technique improves computational efficiency. In essence, the coarse grid gives rapid wave propagation and thus rapid convergence of the solution while the fine grid insures accuracy.

For simplicity, the present method will be described only in a two-dimensional Cartesian coordinate system. It can be easily extended to cover the case of three-dimensional flow problems on general (nonorthogonal) curvilinear meshes.

Governing Equations

The unsteady two-dimensional Euler equations can be written in conservation law form as

$$\frac{\partial U}{\partial t} = - \left[\frac{\partial F}{\partial x} + \frac{\partial G}{\partial y} \right] \tag{1}$$

where

$$U = \begin{vmatrix} \rho \\ \rho u \\ \rho v \\ e \end{vmatrix}, \quad F = \begin{vmatrix} \rho u \\ \rho u u + p \\ \rho u v \\ \rho u h_0 \end{vmatrix}, \quad G = \begin{vmatrix} \rho v \\ \rho v u \\ \rho v v + p \\ \rho v h_0 \end{vmatrix} \tag{2}$$

and

$$h_0 = \frac{e+p}{\rho} = \frac{\gamma}{\gamma-1} \frac{p}{\rho} + \frac{1}{2}(u^2 + v^2) \tag{3}$$

In the above equations, ρ is the density, u and v the velocity components corresponding to the x and y coordinates, e the total internal energy per unit volume, p the pressure, h_0 the total enthalpy, and γ the specific heat ratio.

By knowing the initial and boundary conditions for flow around given obstacles, Eq. (1) can be integrated to provide the inviscid rotational (and/or irrotational) solution at a later time level. Since the flow at steady state is a special case of unsteady flow, the steady-flow solution can also be obtained through solving the unsteady Euler equations.

If homoenergetic steady flow (h_0 = const) is of interest, the energy equation can be eliminated from the solution procedure and the pressure then determined directly from Eq. (3). The results presented here are obtained without solving the energy equation.

New Second-Order Finite Volume Integration Method

Except for very simple cases, solutions of the Euler equations are determined numerically. From the geometries of given flow obstacles, a computational grid is first constructed. The flow properties at each grid point are assigned according to an initial flow condition. The governing equations are then integrated numerically over each subdomain defined by the grid.

In the present work, the integration method used has two basic features. First, the spatial approximation to the governing equation is applied to non-overlapping control volumes to accurately model the law of physics. The other is that the corrections of flow properties at each grid point are deter-

mined by "distribution" formulas. These formulas not only result in a second-order accurate integration method, but, most importantly, provide physical insight into the solution procedure.

Distribution Formulas

The derivation of the distribution formulas and the description of the resultant integration method can be best illustrated through following one-dimensional model equation

$$\frac{\partial U}{\partial t} = -\frac{\partial F(U)}{\partial x} \tag{4}$$

An explicit one-step second-order difference approximation to the above equation, in terms of correction $(\delta U_i = U_i^{n+1} - U_i^n)$, can be expressed as

$$\delta U_i \cong \left(\frac{\partial U}{\partial t}\right)_i^n \Delta t + \left(\frac{\partial^2 U}{\partial t^2}\right)_i^n \frac{\Delta t^2}{2} \cong (F_{i-1}^n - F_{i+1}^n) \frac{\Delta t}{2\Delta x}$$

$$- \left[\left(\frac{\partial F}{\partial U}\right)_{i+\frac{1}{2}}^n (F_i^n - F_{i+1}^n) \frac{\Delta t}{\Delta x}\right.$$

$$\left. - \left(\frac{\partial F}{\partial U}\right)_{i-\frac{1}{2}}^n (F_{i-1}^n - F_i^n) \frac{\Delta t}{\Delta x}\right] \frac{\Delta t}{2\Delta x} \tag{5}$$

where subscript i is the grid index and superscript n refers to the time level. In deriving the above expression, the term $\partial^2 U/\partial t^2$ is replaced by $-(\partial/\partial x)[(\partial F/\partial U)(\partial U/\partial t)]$ based upon Eq. (4).

Because it required a number of numerical operations, the approximation given by Eq. (5) is not, in general, implemented for solving the model equation. However, by defining

$$\Delta U_B = (F_{i-1}^n - F_i^n) \frac{\Delta t}{\Delta x}$$

$$\Delta U_C = (F_i^n - F_{i+1}^n) \frac{\Delta t}{\Delta x}$$

and

$$\Delta F \equiv \left(\frac{\partial F}{\partial U}\right) \Delta U$$

Eq. (5) can be arranged into

$$\delta U_i = \frac{1}{2}\left[\Delta U_B + \frac{\Delta t}{\Delta x}\Delta F_B\right] + \frac{1}{2}\left[\Delta U_C - \frac{\Delta t}{\Delta x}\Delta F_C\right]$$

where subscript B refers to the control volume lying between grid point $i-1$ and i and subscript C refers to the control volume lying between points i and $i+1$, as shown in Fig. 1. This relation implies that the correction to point i is composed of two parts. The first part,

$$(\delta U_i)_B \equiv \frac{1}{2}\left[\Delta U_B + \frac{\Delta t}{\Delta x}\Delta F_B\right] \tag{6}$$

is the correction due to the "change" ΔU_B taking place in the control volume B just upstream of the point i. The other,

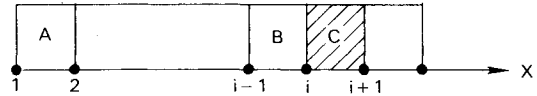$$(\delta U_i)_C \equiv \frac{1}{2}\left[\Delta U_C - \frac{\Delta t}{\Delta x}\Delta F_C\right] \tag{7}$$

Fig. 1   Control volumes used in model one-dimensional problem.

is the correction associated with the change ΔU_C occurring in the downstream control volume C. Now, if the same procedure [Eqs. (5-7)] is applied to grid point $i+1$, one finds that $(\delta U_{i+1})_C$ is

$$(\delta U_{i+1})_C \equiv \frac{1}{2}\left[\Delta U_C + \frac{\Delta t}{\Delta x}\Delta F_C\right]$$

It is interesting to observe that the only difference between $(\delta U_{i+1})_C$ and $(\delta U_i)_C$ is the sign in front of the terms $(\Delta t/\Delta x)\Delta F_C$, which is related to unsteady flux. Adding $(\delta U_i)_C$ and $(\delta U_{i+1})_C$ yields

$$(\delta U_i)_C + (\delta U_{i+1})_C \equiv \Delta U_C$$

which is the change taking place in the control volume C.

With the above findings, a control volume centered integration method is devised and employs the next three operations. For example, at each control volume, say C,

1) Approximate the governing equation by

$$\Delta U_C = \frac{\Delta t}{\Delta x}(F_i^n - F_{i+1}^n) \tag{8}$$

where ΔU_C is called the "change."

2) Determine the corrections to point i and $i+1$ through the use of the "distribution" formulas

$$(\delta U_i)_C = \frac{1}{2}\left[\Delta U_C - \frac{\Delta t}{\Delta x}\Delta F_C\right]$$

$$(\delta U_{i+1})_C = \frac{1}{2}\left[\Delta U_C + \frac{\Delta t}{\Delta x}\Delta F_C\right] \tag{9}$$

in which $\Delta F_C \equiv (\partial F/\partial U)_C \Delta U_C$ and $\partial F/\partial U$ is the Jacobian of F.

3) Update the dependent variable by

$$U_i^{n+1} = U_i^n + \delta U_i$$

$$\delta U_i = (\delta U_i)_B + (\delta U_i)_C \tag{10}$$

when both $(\delta U_i)_B$ and $(\delta U_i)_C$ are known.

The integration method described above is second-order accurate in both space and time. Because it is an explicit numerical procedure, the size of the time step is governed by the Courant-Friedrichs-Lewi (CFL) condition, i.e.,

$$\Delta t \leq \frac{\Delta x}{|W|} \tag{11}$$

where W is the wave speed.

Interpretation of the Distribution Formulas

The distribution formulas [Eqs. (9)] used in the present method can be viewed as the systematic tools for determining the corrections to the surrounding grid points $[(\delta U_i)_C$ and $(\delta U_{i+1})_C]$ due to the change taking place in a control volume (ΔU_C). These formulas provide physical insight into explicit

numerical procedures for solving hyperbolic equations. As a demonstration, the present method is applied to a simple wave equation of the form

$$\frac{\partial U}{\partial t} = -W\frac{\partial U}{\partial x}$$

In this case, the distribution formulas reduce to

$$(\delta U_i)_C = \frac{1}{2}\Delta U_C\left[1 - \frac{\Delta t}{\Delta x}W\right]$$

and

$$(\delta U_{i+1})_C = \frac{1}{2}\Delta U_C\left[1 + \frac{\Delta t}{\Delta x}W\right]$$

where $\Delta U_C = (\Delta t/\Delta x)W(U_i - U_{i+1})$ and $\Delta t/\Delta x \le 1/|W|$, based upon Eqs. (8) and (11), respectively.

An interesting phenomenon can be observed from these two results. When a downstream wave ($W>0$) is lying between points i and $i+1$, the correction applied to the downstream point $i+1$ is greater (in an absolute sense) than that to the upstream point i, i.e.,

$$|(\delta U_{i+1})_C| > |(\delta U_i)_C|$$

whereas for an upstream wave ($W<0$), the opposite of the above expression is true. These conclusions are in accord with wave propagation phenomena. In other words, the distribution formulas are consistent with local wave characteristics. From a numerical point of view, the use of the distribution formulas to provide corrections has an effect similar to the use of upwind or downwind differences, which is necessary to ensure the proper domain of dependence.

One advantage of the present method lies in the simple implementation of nonreflective boundary condition: waves are assumed to propagate out of the boundaries. Since the distribution formulas are consistent with the local wave propagation, the total correction to upstream boundary point 1, for example, is the correction due only to the first control volume A (see Fig. 1),

$$\delta U_1 = (\delta U_1)_A$$

### Numerical Equations for Two-Dimensional Euler Equations

The procedure described above provides the basis with which to form a second-order accurate finite volume integration method for solving the two-dimensional Euler equations. For instance, the solution on a rectangular Cartesian mesh is advanced in time by Δt through the use of the following equations.

The governing equation (1) is first replaced by the finite volume approximation,

$$\Delta U_C = \left[\frac{F_1+F_2}{2}\Delta Y - \frac{F_3+F_4}{2}\Delta Y\right.$$
$$\left. + \frac{G_1+G_4}{2}\Delta X - \frac{G_2+G_3}{2}\Delta X\right]\frac{\Delta t}{\Delta X\Delta Y} \tag{12}$$

where C refers to the control volume defined by grid points 1-4 as shown in Fig. 2a. In Eq. (12), the four terms in the square bracket are the fluxes crossing the four faces of the control volume.

The corrections to the grid points, associated with the
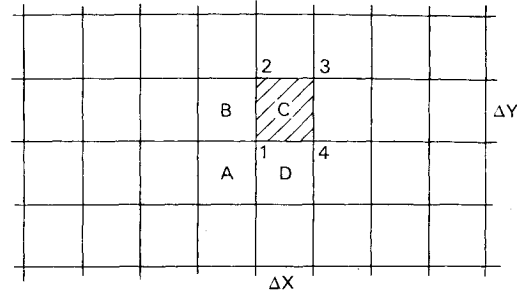
a) Fine mesh (h grid).
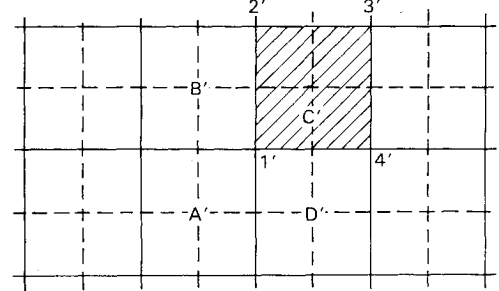
b) Coarse mesh ($2h$ grid).

Fig. 2   Control volumes used in two-dimensional problem.

control volume C, are determined by the two-dimensional distribution formulas, i.e.,

$$(\delta U_1)_C = \frac{1}{4}\left[\Delta U_C - \frac{\Delta t}{\Delta x}\Delta F_C - \frac{\Delta t}{\Delta y}\Delta G_C\right]$$

$$(\delta U_2)_C = \frac{1}{4}\left[\Delta U_C - \frac{\Delta t}{\Delta x}\Delta F_C + \frac{\Delta t}{\Delta y}\Delta G_C\right]$$

$$(\delta U_3)_C = \frac{1}{4}\left[\Delta U_C + \frac{\Delta t}{\Delta x}\Delta F_C + \frac{\Delta t}{\Delta y}\Delta G_C\right] \tag{13}$$

$$(\delta U_4)_C = \frac{1}{4}\left[\Delta U_C + \frac{\Delta t}{\Delta x}\Delta F_C - \frac{\Delta t}{\Delta y}\Delta G_C\right]$$

in which $\Delta F_C \equiv (\partial F/\partial U)_C\Delta U_C$ and $\Delta G_C \equiv (\partial G/\partial U)_C\Delta U_C$ are the unsteady fluxes with $\partial F/\partial U$ and $\partial G/\partial U$ being the Jacobians of F and G. (Explicit expressions for ΔF and ΔG are given in Appendix A.)

The flow properties at point 1 are then updated by

$$U_1^{n+1} = U_1^n + \delta U_1$$
$$\delta U_1 = (\delta U_1)_A + (\delta U_1)_B + (\delta U_1)_C + (\delta U_1)_D \tag{14}$$

where A-D refer to control volumes surrounding the grid point 1 (see Fig. 2a). The stability condition of the explicit two-dimensional Euler solver is

$$\Delta t \le \min\left(\frac{\Delta x}{|u|+a}, \frac{\Delta y}{|v|+a}\right)$$

in which $a = \sqrt{\gamma p/\rho}$ is the speed of sound.

These numerical equations can be applied to obtain inviscid solutions for subsonic, transonic, and supersonic flow problems. However, it is found that, for transonic and supersonic applications, artificial viscous damping should be introduced into the solution procedure to stabilize "captured" shocks. In the present work, the effect of artificial viscosity is provided by adding smoothing terms in the

distribution formulas (13). For example, after including the numerical smoothing term, the formula for $(\delta U_I)_C$ becomes

$$(\delta U_I)_C = \frac{1}{4}\left[\Delta U_C - \frac{\Delta t}{\Delta x}\Delta F_C - \frac{\Delta t}{\Delta y}\Delta G_C + \mu(\bar{U} - U_I)\right] \quad (15)$$

where

$$\bar{U} \equiv \tfrac{1}{4}(U_1 + U_2 + U_3 + U_4)$$

$$\mu = \sigma\left(\frac{\Delta t}{\Delta x} + \frac{\Delta t}{\Delta y}\right)$$

and σ is an artificial damping factor taking value between 0.0 and 0.1.

The preceding method uses finite volume approximation to discretize the governing equations so that the "change" occurring in each non-overlapping control volume can be accurately provided. The use of the two-dimensional distribution formulas to determine the "corrections" to the grid points then automatically insures the proper domain of dependence regardless of local flow direction and wave speed, and thus leads to a stable second-order finite volume integration method. With slight modifications to the flux terms in Eqs. (12) and (13), the present method can be extended to address flow problems on general curvilinear meshes. In Appendix B the numerical equations for nonorthogonal two-dimensional mesh are given.

Multiple-Grid Scheme

To reduce the computational time, one would like to use a coarse grid system with which the numbers of unknowns are relatively large. However, the solution obtained from the coarser level of discretization is usually not sufficiently accurate due to large truncation errors. One way to overcome this is to use the "multiple-grid" technique[5] wherein the solution on the fine grid is obtained by cycling the numerical procedure between fine and coarser grid systems. The basic idea behind the multiple-grid technique is the use of coarser grids to propagate the fine grid corrections properly and rapidly throughout the field, thus improving convergence rate to steady state while maintaining low truncation errors.

To implement this technique, coarser grid systems have to be generated. In the present work, the coarse grid is obtained by removing every other line in the fine mesh as shown in Fig. 2b. Recognizing that the corrections are due to wave movements and the distribution formulas are the systematic tools to propagate these waves, a simple multiple-grid scheme for solving the Euler equations is constructed by combining the new integration method with the following coarser grid solution procedure.

Instead of the finite-volume approximation as given in Eq. (12), the change, ΔU^{2h}, occurring in control volumes of $2h$ grid are determined by

$$\Delta U^{2h} = T_h^{2h} \delta U^h \quad (16)$$

where T_h^{2h} is an operator which transfers to each control volume of the coarse grid the correction δU^h of the centered fine grid point, or alternatively a weighted average of the corrections at those fine grid points defining the coarse control volume. The generalized distribution formulas

$$(\delta U_{1'})_{C'} = \frac{1}{4}\left[\Delta U_{C'}^{2h} - \frac{\Delta t}{\Delta x}\Delta F_{C'}^{2h} - \frac{\Delta t}{\Delta y}\Delta G_{C'}^{2h}\right]$$

$$(\delta U_{2'})_{C'} = \frac{1}{4}\left[\Delta U_{C'}^{2h} - \frac{\Delta t}{\Delta x}\Delta F_{C'}^{2h} + \frac{\Delta t}{\Delta y}\Delta G_{C'}^{2h}\right]$$

$$(\delta U_{3'})_{C'} = \frac{1}{4}\left[\Delta U_{C'}^{2h} + \frac{\Delta t}{\Delta x}\Delta F_{C'}^{2h} + \frac{\Delta t}{\Delta y}\Delta G_{C'}^{2h}\right]$$

$$(\delta U_{4'})_{C'} = \frac{1}{4}\left[\Delta U_{C'}^{2h} + \frac{\Delta t}{\Delta x}\Delta F_{C'}^{2h} - \frac{\Delta t}{\Delta y}\Delta G_{C'}^{2h}\right]$$

$$(17)$$

are then used to propagate the change $\Delta U_{C'}^{2h}$ to the nearby coarse grid points (points 1'-4' defining the control volume C' as shown in Fig. 2b) and to form the correction of the $2h$ grid, i.e.,

$$\delta U_{I'}^{2h} = (\delta U_{I'})_{A'} + (\delta U_{I'})_{B'} + (\delta U_{I'})_{C'} + (\delta U_{I'})_{D'}$$

After finding δU^{2h} on all coarse grid points, the flow properties at the *finest* grids are updated by

$$U^{new} = U + I_{2h}^h \delta U^{2h} \quad (18)$$

where I_{2h}^h is a linear interpolation operator which interpolates the coarse grid corrections to give the corrections at each grid point on the finest mesh.

The above procedure [Eqs. (16-18)] is repeated on progressively coarser grids until the coarsest grid is reached. The result is a multiple-grid scheme for solving the Euler equations. One iteration cycle of the present multiple-grid scheme (shown in Fig. 3) is composed of one application of the basic integration method [Eqs. (12-14)] to the finest grid and one application of the coarse grid procedure [Eqs. (16-18)] to each level of progressively coarser grids.

The present scheme requires only two levels of storage, one for the dependent variables and the other for the corrections. Both of them are for the finest grid. The truncation error associated with the scheme is at the least second-order on the finest grid because the spatial approximation to the governing equation is applied only on the finest mesh. With the multiple-grid application, the use of the coarser grids minimizes the computation work needed to propagate the unsteady waves out of computational domain so that a steady state is rapidly reached.

Results

The numerical method described in the last two sections has been coded and tested on a variety of flow problems. Com-
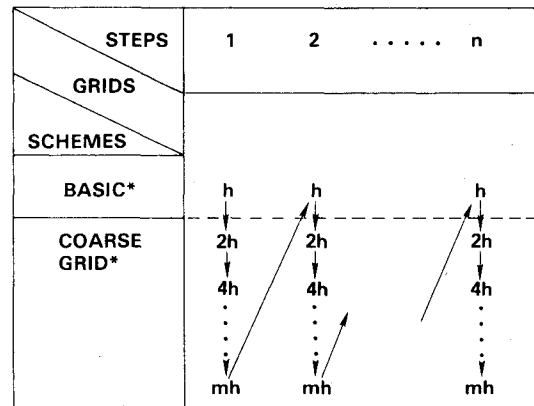
*EQS. (12) to (14)
**EQS. (16) to (18)

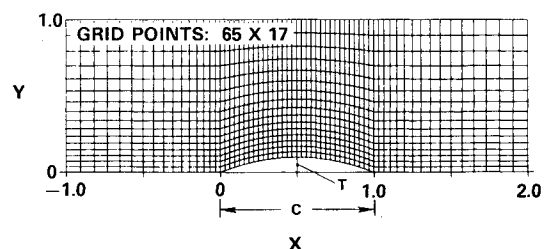Fig. 3　Computation sequence for the present multiple-grid scheme.

Fig. 4　Computation mesh for the channel flow with a 10% thick circular arc bump.

puted results indicate that the present scheme is accurate, reliable, and fast. Some of the numerical results are given here to demonstrate the capability and efficiency of the present multiple-grid Euler solver.

Figure 4 shows the computational mesh, composed of 65×17 points, being used in both subsonic and transonic calculations for flow in a channel with a circular arc "bump" on the lower wall. The width of the channel is equal to the length of the bump and the thickness-to-chord ratio of the bump is 10%. This geometry is identical to the test case used in Ref. 6. For both calculations, the flow in the channel is initially uniform having the far upstream flow properties and then the flow tangency condition for the walls and nonreflective condition for both *upstream* and *downstream* boundaries are applied after each time step. The solution is assumed to reach steady state when average absolute corrections of normalized X momentum (ρu) is less than 1×10^{-5}.

Figure 5 presents the Mach number distribution and isomach lines of the steady flow solution at $M_{-\infty} = 0.5$. As shown in the figure, the numerical solution is quite symmetric about the midchord, which is a good indication of solution accuracy for this subsonic application. From the calculation $M_{-\infty} = 0.675$, a supersonic region appears in the solution which is terminated by a shock as shown in Figs. 6a and 6b. The captured shock is located around 72% of chord and spread over three grid points. The flow behind the shock is rotational and thus the isomach lines downstream of the shock no longer intersect the lower flat wall at right angles as seen in Fig. 6b. Figure 6c shows the total pressure loss $[\Delta P_T = 1(P_T/P_{T-\infty})]$ contours for this case. In the region of shock smearing, the loss reaches maximum value at the middle shock point which is manifested as an island in the loss contour. However, it can be seen that the lines of constant loss behind the shock follow the streamlines, as they should for an inviscid rotational flow.

Figure 7 presents the convergence histories of this transonic calculation. One of them is obtained by executing the basic integration method without the multiple-grid capability. It is shown that the basic integration method requires more than 900 steps for the solution to reach "steady" state. With the help of multiple-grid scheme, the same steady solution (different only in the fourth significant digit) is obtained after 135 steps. The CPU time is about 25 s for the run with the multiple-grid scheme and 120 s without it on IBM 3033 computer. The savings in computational time is about 80% for this test case.

Figure 8 presents the solution for a supersonic flow $(M_{-\infty} = 1.4)$ past a 4% thick circular arc bump in the channel.

Both initial and boundary conditions applied to this supersonic test case are the same as in previous two cases. It can be seen that two oblique shocks are formed at both corners of the bump. The leading-edge oblique shock is weakened by the expansion waves emitted from the convex surface of the bump and traveling across the channel. This shock is spread numerically over five grid points before reaching the upper wall and then is reflected back by the wall into the expanding flowfield. The shock reflection and weakening is clearly seen in the loss contours of Fig. 8c. The trailing-edge shock is also weakened by the expansion waves associated with the bump and then going out of the computational domain. It takes about 20 s to compute this solution on the 65×17 grid.
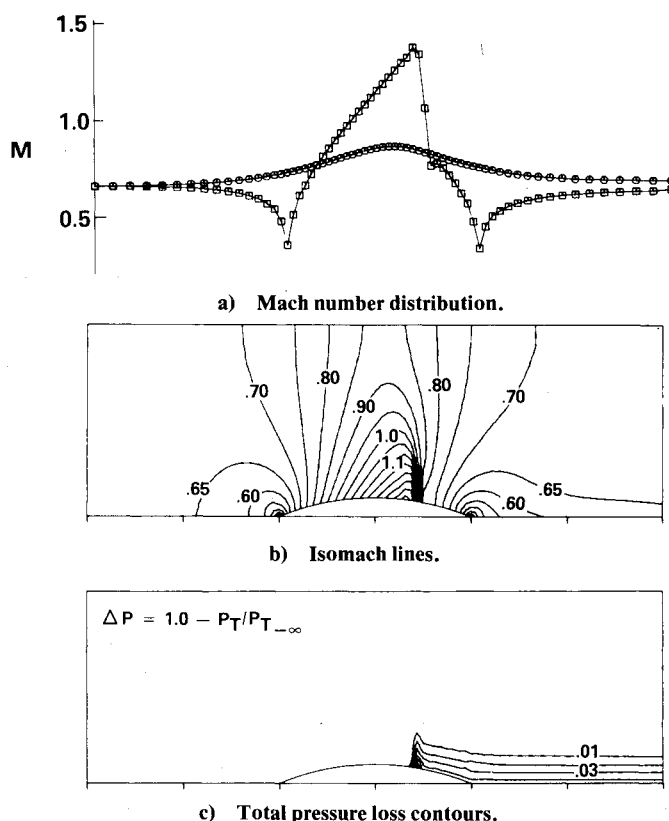

a)   Mach number distribution.

b)   Isomach lines.

$\Delta P = 1.0 - P_T/P_{T-\infty}$

c)   Total pressure loss contours.

Fig. 6   Transonic solution for flow in the channel at $M_{-\infty} = 0.675$.

a)   Mach number distribution.

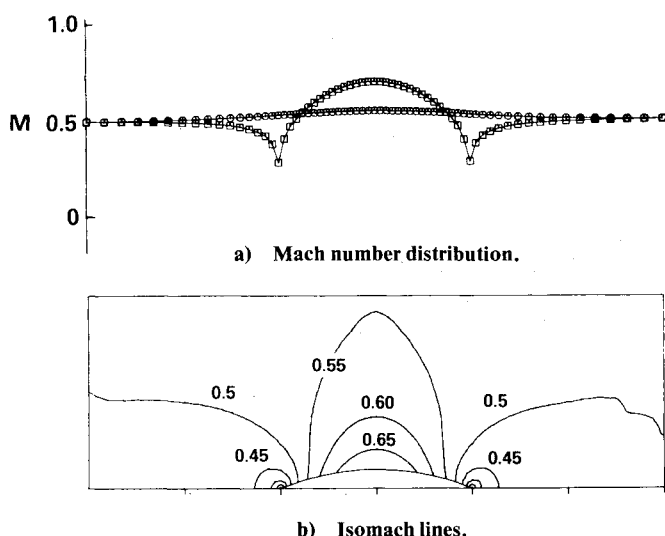b)   Isomach lines.

Fig. 5   Subsonic solution for flow in the channel at $M_{-\infty} = 0.5$.
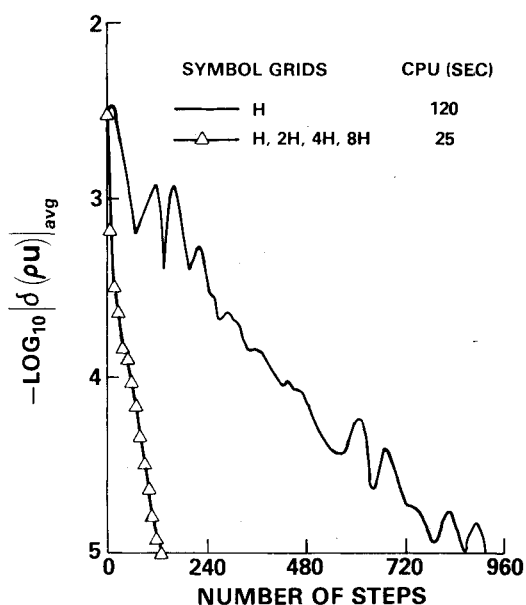

Fig. 7   Convergence history for transonic flow in the channel.

Figure 9a shows part of the curvilinear mesh used in obtaining the transonic solution for flow around an axisymmetric nacelle with a centerbody. This grid is generated by the conformal mapping technique of Ref. 7. A nonreflective boundary condition is used for the exterior far

a) **Mach number distribution.**

b) **Isomach lines.**

c) **Total pressure loss contours.**

Fig. 8 Supersonic solution for flow in a channel with a 4% thick circular arc bump, $M_{-\infty} = 1.4$.

field, the flow tangency condition is applied on the solid surfaces, and static pressure is held constant at interior downstream boundary. A far-field Mach number of 0.77 and capture ratio of 0.66 are used in this transonic axisymmetric flow calculation. The computed Mach number distribution on the cowl is shown in Fig. 9b, along with solutions determined by a fully conservative transonic potential solver.[8] Two potential solutions are given, one is obtained on the same 65 × 17 grid used by the present Euler solver and the other on a finer mesh consisting of 129 × 33 points. It can be seen that all three solutions agree well around leading-edge stagnation point but the Euler solution obtained from the coarse grid matches better with the finer potential solution along inner surface of the cowl and ahead of the shock. The shock captured by the Euler solver is ahead of the shocks captured by the potential flow solver for this case. This is because the Euler formulation conserves both mass and momentum, while potential formulation conserves mass only and results in a momentum increase across the shock. This increase in momentum is also manifested in the higher level of the Mach number downstream of the shock by the potential solver. For this test case, the Euler method takes 35 s to generate the solution and the potential method uses 15 s for the coarse grid solution and an additional 45 s for the fine grid solution.

Figure 10 presents the solution for flow past the VKI gas turbine rotor blades[9] at an upstream Mach number of 0.270 and at an angle of 60 deg. The flow is turned about 96 deg by the blades and exits to a downstream static pressure corresponding to a isentropic Mach number of 1.11. As shown in Fig. 10, agreement between computed results and experimental data is good along the pressure surface, but the calculated Mach number is slightly higher on the suction surface before shock impingement. The shock is generated at the trailing edge of the blade above as demonstrated in the Mach contours (Fig. 10b). A schlieren photograph from the test[9] indicates that the shock is formed somewhat downstream
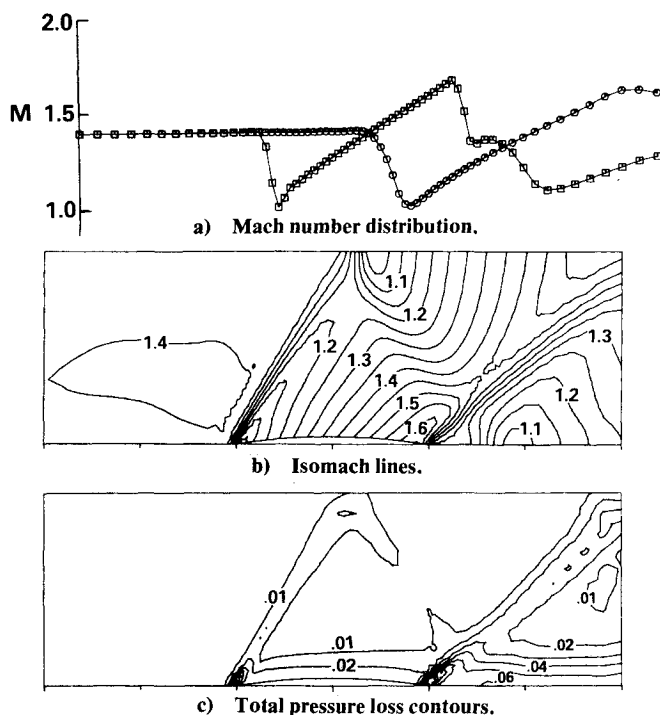

a) **Computation mesh.**

b) **Mach number distribution along the cowl.**

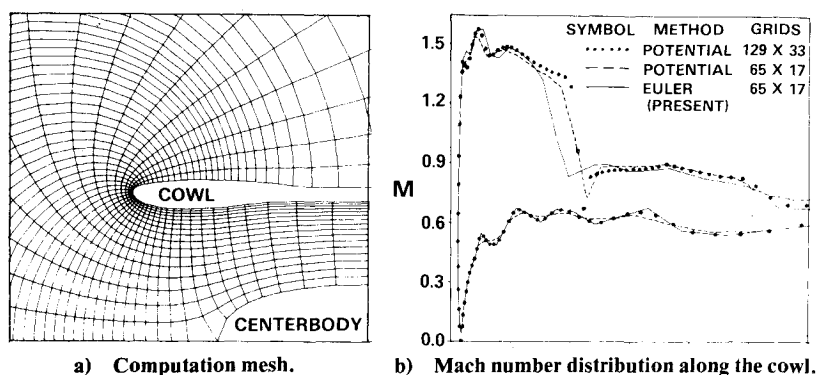**Fig. 9 Transonic solution for flow around an axisymmetric nacelle with a centerbody, $M_{-\infty} = 0.77$ and MFR = 0.66.**

a) **Mach number distribution.**

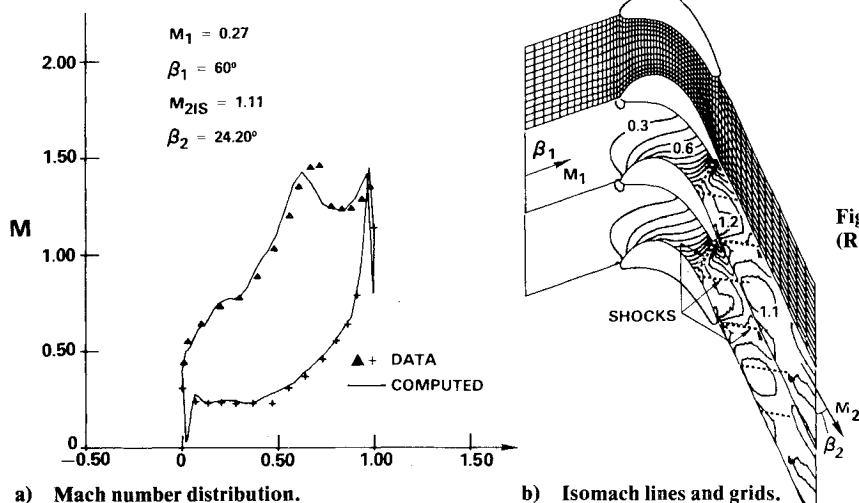

b) **Isomach lines and grids.**

Fig. 10 Flow past VKI gas turbine rotor blades (Ref. 9).

of the trailing edge due to sudden growth of boundary layer around that region. Therefore, the predicted shock location is ahead of actual shock locations. For this case, it takes about 20 s to obtain the solution on a 65×13 grid.

Conclusions

This paper presents a new second-order accurate finite volume method for solving the unsteady Euler flow equations. To arrive at this second-order integration method, special "distribution" formulas, consistent with local wave characteristics, are utilized. These formulas are found to provide physical insight into solution procedure. With the help of these formulas, a simple multiple-grid scheme is constructed and leads to a fast explicit numerical procedure for determining the *steady* solutions of the Euler equations. The present scheme has been applied to both internal and external flow problems at subsonic, transonic, and supersonic speeds. Numerical results indicate that the present multiple-grid Euler solver is an accurate, reliable, and fast method for predicting the inviscid rotational (and/or irrotational) solution for flow around a variety of obstacles.

Appendix A: Expressions for ΔF and ΔG

Finite volume approximation of the governing equations leads to values of change ΔU, i.e.,

$$\Delta U = \begin{vmatrix} (\Delta \rho) \\ (\Delta \rho u) \\ (\Delta \rho v) \\ (\Delta e) \end{vmatrix}$$

Therefore, ΔF and ΔG can be obtained by following expressions

$$\Delta F = \left(\frac{\partial F}{\partial U} \right) \Delta U = \begin{vmatrix} (\Delta \rho u) \\ u(\Delta \rho u) + u(\rho \Delta u) + \Delta P \\ v(\Delta \rho u) + u(\rho \Delta v) \\ h_0 (\Delta \rho u) + u(\rho \Delta h_0) \end{vmatrix} \quad \text{(A1)}$$

$$\Delta G = \left(\frac{\partial G}{\partial U} \right) \Delta U = \begin{vmatrix} (\Delta \rho v) \\ u(\Delta \rho v) + v(\rho \Delta u) \\ v(\Delta \rho v) + v(\rho \Delta v) + \Delta P \\ h_0 (\Delta \rho v) + v(\rho \Delta h_0) \end{vmatrix} \quad \text{(A2)}$$

where

$$(\rho \Delta u) = (\Delta \rho u) - u(\Delta \rho)$$
$$(\rho \Delta v) = (\Delta \rho v) - v(\Delta \rho)$$
$$(\Delta P) = (\gamma - 1) \left\{ (\Delta e) - \frac{1}{2} \left[u(\Delta \rho u) + v(\Delta \rho v) \right. \right.$$
$$\left. \left. + u(\rho \Delta u) + v(\rho \Delta v) \right] \right\}$$
$$(\rho \Delta h_0) = (\Delta e) + (\Delta P) - h_0 (\Delta \rho)$$

Appendix B: Numerical Equations for a General Two-Dimensional Mesh

Finite Volume Approximation

$$\Delta U_C = \frac{\Delta t}{\Delta V} \left\{ \left[\frac{F_1 + F_2}{2} (y_2 - y_1) - \frac{G_1 + G_2}{2} (x_2 - x_1) \right] \right.$$
$$- \left[\frac{F_3 + F_4}{2} (y_3 - y_4) - \frac{G_3 + G_4}{2} (x_3 - x_4) \right]$$
$$+ \left[\frac{G_1 + G_4}{2} (x_4 - x_1) - \frac{F_1 + F_4}{2} (y_4 - y_1) \right]$$
$$\left. - \left[\frac{G_2 + G_3}{2} (x_3 - x_2) - \frac{F_2 + F_4}{2} (y_3 - y_2) \right] \right\} \quad \text{(B1)}$$

$$\Delta V = -0.5 [(x_3 - x_1) (y_4 - y_2) - (x_4 - x_2) (y_3 - y_1)] \quad \text{(B2)}$$

where subscript C refers to control volume surrounded clockwisely by grid points 1-4.

Distribution Formulas

$$(\delta U_1)_C = \frac{1}{4} [\Delta U_C - \Delta f_C - \Delta g_C]$$
$$(\delta U_2)_C = \frac{1}{4} [\Delta U_C - \Delta f_C + \Delta g_C]$$
$$(\delta U_3)_C = \frac{1}{4} [\Delta U_C + \Delta f_C + \Delta g_C] \quad \text{(B3)}$$
$$(\delta U_4)_C = \frac{1}{4} [\Delta U_C + \Delta f_C - \Delta g_C]$$

where

$$\Delta f_C = \frac{\Delta t}{\Delta v} (\Delta F_C \Delta y^\ell - \Delta G_C \Delta x^\ell)$$
$$\Delta g_C = \frac{\Delta t}{\Delta v} (\Delta G_C \Delta x^m - \Delta F_C \Delta y^m) \quad \text{(B4)}$$

with

$$\Delta x^\ell = 0.5 * (x_2 + x_3 - x_1 - x_4)$$
$$\Delta y^\ell = 0.5 * (y_2 + y_3 - y_1 - y_4)$$
$$\Delta x^m = 0.5 * (x_3 + x_4 - x_1 - x_2) \quad \text{(B5)}$$
$$\Delta y^m = 0.5 * (y_3 + y_4 - y_1 - y_2)$$

Time Step

$$\Delta t \leq \min \left(\frac{\Delta V}{|u \Delta y^\ell - v \Delta X^\ell| + a \Delta \ell}, \frac{\Delta V}{|u \Delta y^m - v \Delta x^m| + a \Delta m} \right) \quad \text{(B6)}$$

in which

$$\Delta \ell = \sqrt{(\Delta x^\ell)^2 + (\Delta y^\ell)^2}, \qquad \Delta m = \sqrt{(\Delta x^m)^2 + (\Delta y^m)^2}$$

Acknowledgment

References

[1] MacCormack, R. W., "The Effects of Viscosity in Hypervelocity Impact Cratering," AIAA Paper 60-345, May 1969.

[2] McDonald, P. W., "The Computation of Transonic Flow Through Two-Dimensional Gas Turbine Cascades," ASME Paper 71-GT-89, April 1971.

[3] Denton, J. E., "A Time-Marching Method for Two- and Three-Dimensional Blade-to-Blade Flows," Aeronautical Research Council, British R&M No. 3775, Oct. 1974.

[4] Turkel, E., "On the Practical Use of High Order Methods for Hyperbolic Systems," ICASE Rept. 78-19, 1978.

[5] Brandt, A., "Multi-Level Adaptive Computations in Fluid Dynamics," AIAA Paper 79-1455, 1979.

[6] Moretti, G., "Experiments on Initial and Boundary Conditions," Paper presented at Symposium on Numerical and Physical Aspects of Aerodynamic Flow, Jan. 1981.

[7] Ives, D. C. and Menor, W. A., "Mesh Generation for Inlet and Inlet-Centerbody Configurations Using Conformal Mapping and Stretching," AIAA Paper 81-0997, 1981.

[8] Jameson, A., Private communication, Dec. 1979.

[9] Sieverding, C. H., "Experimental Data on Two Transonic Turbine Blade Sections and Comparison with Various Theoretical Methods," Von Kármán Institute for Fluid Dynamics, Rept. LS59, 1973.